Cell Death & Differentiation (2021) 28:915–931
https://doi.org/10.1038/s41418-020-00625-7

Cell Death & Differentiation

ARTICLE

Genetic inactivation of RIP1 kinase does not ameliorate disease in a mouse model of ALS

Sara Dominguez[1] · Eugene Varfolomeev[2] · Robert Brendza[1] · Kim Stark[1] · Joy Tea[1] · Jose Imperio[1] · Hai Ngu[3] · Timothy Earr[1] · Oded Foreman[3] · Joshua D. Webster[3] · Amy Easton[1] · Domagoj Vucic[2] · Baris Bingol[1]

Received: 29 July 2020 / Revised: 7 September 2020 / Accepted: 11 September 2020 / Published online: 29 September 2020

Abstract

RIP1 kinase is proposed to play a critical role in driving necroptosis and inflammation in neurodegenerative disorders, including Amyotrophic Lateral Sclerosis (ALS). Preclinical studies indicated that while pharmacological inhibition of RIP1 kinase can ameliorate axonal pathology and delay disease onset in the mutant SOD1 transgenic (SOD1-Tg) mice, genetic blockade of necroptosis does not provide benefit in this mouse model. To clarify the role of RIP1 kinase activity in driving pathology in SOD1-Tg mice, we crossed SOD1-Tgs to RIP1 kinase-dead knock-in mice, and measured disease progression using functional and histopathological endpoints. Genetic inactivation of the RIP1 kinase activity in the SOD1-Tgs did not benefit the declining muscle strength or nerve function, motor neuron degeneration or neuroinflammation. In addition, we did not find evidence of phosphorylated RIP1 accumulation in the spinal cords of ALS patients. On the other hand, genetic inactivation of RIP1 kinase activity ameliorated the depletion of the neurotransmitter dopamine in a toxin model of dopaminergic neurodegeneration. These findings indicate that RIP1 kinase activity is dispensable for disease pathogenesis in the SOD1-Tg mice while inhibition of kinase activity may provide benefit in acute injury models.

Introduction

Receptor-interacting protein (RIP) kinases are key modulators of cell death, cell survival, and inflammatory signaling [1]. RIP1 and RIP3 kinases play a central role in determining cell fate in complex signaling pathways initiated by a variety of stimuli including tumor necrosis factor (TNF) receptor activation, cellular stress, and infection. In these pathways, RIP1 functions both as a scaffolding protein to promote cell survival and inflammatory gene expression, and as a kinase to promote inflammatory cell death [2]. In particular, kinase-active RIP1, marked by autophosphorylation on S166 [3–5], drives both caspase-8-dependent apoptosis and RIP3-dependent necroptosis [6]. When caspase-8 is not adequately activated, RIP1 kinase drives necroptosis by recruiting RIP3, which stimulates RIP3 autophosphorylation [7–9]. RIP3 then phosphorylates and promotes the activation of the pseudokinase mixed lineage kinase-like (MLKL) [10], which in turn oligomerizes and disrupts the integrity of plasma membrane [11, 12]. Importantly, genetic or pharmacological inhibition of RIP1 kinase decreases pathogenesis in animal models driven by inflammation and cell death [1, 13, 14], including in models of tissue injury and neurodegenerative disease [5, 14–26]. Together, these studies highlight the potential of RIP1 kinase inhibition as a therapeutic approach for diverse inflammatory, infectious, and neurodegenerative diseases [1, 2, 27].

Amyotrophic Lateral Sclerosis (ALS) is a young adult-onset and progressive neurodegenerative disorder characterized by degeneration of motor neurons in the motor cortex and the spinal cord [28]. Recent studies suggest that kinase activity of RIP1 may have a key role in driving

Edited by D.L. Vaux

Supplementary information The online version of this article (https://doi.org/10.1038/s41418-020-00625-7) contains supplementary material, which is available to authorized users.

✉ Baris Bingol
barisb@gene.com

[1] Department of Neuroscience, Genentech, Inc., South San Francisco, CA 94080, USA

[2] Department of Early Discovery Biochemistry, Genentech, Inc., South San Francisco, CA 94080, USA

[3] Department of Pathology, Genentech, Inc., South San Francisco, CA 94080, USA

neurodegeneration in ALS by promoting inflammation and demyelination [25], and astrocyte-driven toxicity [24, 29]. In particular, depletion of genes linked to ALS, Optineurin (*OPTN*) [30–32] and Tank Binding Kinase 1 (*TBK1*) [31, 33], may cause axonal pathology and inflammation by promoting overactivation of RIP1 kinase. In addition, axonal pathology in mutant SOD1-Tg(G93A) mouse, an established model of ALS, [34, 35], is ameliorated by genetic depletion of RIP3 or by pharmacological inhibition of RIP1 [25]. Further supporting RIP pathway as a target for ALS, the abundance of pRIP1(S14,15), and total protein levels of RIP1, RIP3, and MLKL are increased in spinal cords of ALS patients compared to healthy individuals [25].

Of note, other studies questioned the significance of necroptosis in ALS pathogenesis [29, 36]. In particular, deletion of MLKL [36] or RIP3 [29] did not provide benefit in motor neuron degeneration or gliosis, and did not improve disease course or survival in the mutant SOD1-Tg (G93A) mice. In addition, RIP1 abundance did not differ in spinal cords between healthy and ALS individuals [29]. These studies indicate necroptosis is dispensable for disease progression in the SOD1-Tg(G93A) mice.

Given that RIP1 has pleiotropic roles that are independent of RIP3 and MLKL in driving cell death and inflammation [2, 14], the potential benefit of RIP1 kinase inhibition in ameliorating ALS-related pathology remains to be determined. Furthermore, validation of RIP1 as a target for ALS is valuable since the kinase activity of RIP1 is a more tractable target than inhibition of RIP3 kinase or depletion of RIP3/MLKL [2, 37, 38]. To this end, we crossed the mutant SOD1-Tg(G93A) mice with RIP1 (D138N) KD knock-in mice (referred to as "SOD1-Tg x RIP1-KD"), and examined pathway activation and disease progression. Furthermore, we sought evidence of pathway activation in ALS. Our data do not support a role for RIP1 kinase activity in driving pathogenesis in the SOD1-Tg model or the pathway activation in ALS spinal cords. Further experiments in RIP1-KD mice indicated that kinase inhibition is partially beneficial in a toxin model of dopaminergic neuron degeneration. Together, these findings suggest a context-dependent role for RIP1 in driving pathology in neurodegenerative models.

Materials and methods

Mice

SOD1-Tg (G93A) high copy number transgenic mice were originally derived from Jackson Laboratory, Ben Harbor, ME, USA (stock #002726) [39] and were backcrossed at Genentech for >20 generations into C57BL/6N (Charles River, Wilmington, MA, USA). These mice where then crossed to RIP1-KD mice previously described in [38]. A hemizygous breeding design was used to produce littermate mice from all four genotypes. SOD1-Tg copy number calculations of DNA concentration for SOD1(G93A) mice as well as recipes and amplification were described previously [40]. All SOD1(G93A) animals enrolled into the study fell into the expected high copy number ranges as described above. Male and female mice were distributed equally between experimental groups.

Mice were housed on a regular light/dark cycle (14:10 h) with *ad libitum* access to food (LabDiet 5010) and water. All behavioral assessments were conducted during the light phase. All protocols for mouse experiments were approved by the Institutional Animal Care and Use Committee and were conducted in accordance with the NIH Guide for the Care and Use of Laboratory Animals.

Tissue lysis

WT or SOD1-Tg littermate animals (8, 11–12, and 16–17-week-old) were perfused with PBS and spinal cords, cortex and sciatic nerve were collected dissected, weighed and placed on dry ice. Tissue were stored at −80 °C until processed. Following rinsing in cold PBS, tissues were lysed in 10-fold tissue-weight volume (ml/mg) of cold RIPA buffer (150 mM NaCl, 0.1% SDS, 1% Triton X-100, 1% sodium deoxycholate, 50 mM Tris-HCl, pH 7.4 supplemented with protease and phosphatase inhibitors) using TissueLyserII (Qiagen, Hilden, Germany) followed by further extraction via sonication in SDS-lysis buffer (7.5 mM Tris pH 8.0, 1.5% SDS, 7.5% sucrose, 1.5 mM EDTA). Lysates were heated for 10 min at 95 °C, spun at 15000 rpm for 10–20 min, and protein concentrations in the supernatant were determined using detergent-compatible BCA assay (Thermo Fisher, Waltham, MA, USA). Lysates were diluted ~1.5-fold and supplemented with bromophenol blue and 1% DTT before gel electrophoresis. Final protein concentrations were adjusted to 2 mg/ml and 14–20 µg protein were separated by using 4–12% LDS acrylamide gels (Thermo Fisher).

To examine protein expression in different brain regions, tissues were procured from Zyagen, San Diego, CA, USA and lysed in N-Per Neuronal extraction buffer (Thermo Fisher, #87792) supplemented with protease and phosphatase inhibitors followed by extraction with Bead Raptor Homogenizer (OMNI International, Kennesaw, GA, USA). Tissue lysates prepared from peripheral organs were purchased from Zyagen.

Immunoblotting

Proteins were transferred to nitrocellulose membranes and immunoblotted with primary antibodies in 5% milk in

TBST buffer. The primary antibodies used were derived against actin (Cell Signaling Technology, Danvers, MA, USA #3700, AB_2242334), GAPDH (Cell Signaling Technology #5174, AB_10622025), HSP90 (Cell Signaling Technology #4877, AB_2233307), RIP1 (Cell Signaling Technology #3493, AB_2305314 in Fig. 1a, Supplementary Fig. 1C; BD #610459, AB_397832 in Fig. 1e, Supplementary Fig. 1F, I), pRIP1(S166) (Cell Signaling Technology #31122, AB_2799000), RIP3 (Abcam, Cambridge, UK #ab72106, AB_1270322; Bio-Rad, Hercules, CA, USA #AHP1797, AB_2178676; Cell Signaling Technology #13526, AB_2687467 in Supplementary Fig. 1G. Genentech clone 1G6.1.4 in Fig. 1c, e and Supplementary Fig. 1G, I), MLKL (Abcam #ab183770; Abcam #ab172868, AB_2737025; Sigma-Aldrich, St. Louis, MO, USA #SAB1302339, AB_2687464 in Supplementary Fig. 1H. EMD Millipore, Hayward, CA, USA #MABC604, AB_2820284 in Fig. 1d, e and Supplementary Fig. 1H).

TBZ treatment of L929 and HT-29 cells

L929 and HT-29 cells were obtained from the American Type Culture Collection, Manassas, VA, USA. Cell lines are quality controlled by Genentech Cell Bank via STR analysis as well as mycoplasma testing. RIP1 KO and RIP (K45A) KI HT-29 cells were described before [41]. Cells were cultured in 50:50 Dulbecco's modified Eagle's medium and FK12 medium supplemented with 10% fetal bovine serum, penicillin, and streptomycin. Cells were treated with TNF (10 ng/ml), BV6 (1 μM) and zVAD (20 μM) for 3 h. Following this treatment, cells were scraped and lysed in 40 mM Tris-HCl (pH 7.5), 150 mM NaCl, 1 mM EDTA, and 1% Triton X-100 and immunoblotted as described above.

Immunoprecipitation assay for measuring pRIP1 (S166)

To immunoprecipitate RIP1, TBZ-treated L929 cell cultures were lysed as described above and 6 mg of lysates were treated with a mixture of antibodies against RIP1 (BD, San Jose, CA, USA #610459, AB_397832 and Abnova Taipei, Taiwan #MAB0836, AB_1204916, 6 μg each) and 17 μl of protein-A/G magnetic beads (ThermoFisher). To immunoprecipitate RIP1 from SOD1-Tg brain and spinal cord tissues, 8 or 1.3 mg/IP tissue lysates, respectively, were precipitated with a mixture of anti RIP1 antibodies as described above (1 μg per 1 mg lysate of each antibody and 17 μL of protein-A/G magnetic beads (ThermoFisher)). Immunoprecipitated protein complexes were washed several times in lysis buffer, resolved by SDS-polyacrylamide gel electrophoresis (SDS-PAGE) and analyzed by Western blotting with the indicated antibodies.

Compound muscle action potential (CMAP) measurement

CMAP amplitudes were assessed every two weeks from 5–13 weeks of age. Mice were anesthetized with 2.5% isoflurane, right leg and hip were shaved and remaining hair was removed. Two stimulating needle electrodes were inserted perpendicular to the nerve into either side of the right sciatic notch. Recording needle electrodes were inserted into the Achilles tendon (anode) and into either the tibialis anterior (TA) or the gastrocnemius muscle (GA), and a digital ring ground electrode, coated in electrode cream, was placed on the mouse's tail. Data was amplified (BioAmp, ADinstruments, Sydney, Australia) and acquired with a sampling rate of 10 kHz, and filtered at 1 Hz high pass and 5 kHz low pass (Powerlab 4/25, ADInstruments, Sydney, Australia). A controlled stimulus, with a pulse duration of 0.2 ms, was applied to the nerve to evoke contractions from the Tibialis Anterior muscle in 2 mA increments, starting from 2 to as high as 50 mA, until the amplitude no longer increased. The maximum amplitude (in mV) was measured from the maximum negative to the maximum positive peak for each mouse. To determine the conductance latency, the time from initiation of the stimulus to the initiation of the response was measured from each mouse's maximum wave.

Grip strength measurement

Grip strength was measured every two weeks from 6–14 weeks of age and never on the same week as CMAP. Grams of force were collected using dual sensor model, Chatillon Grip Strength meters, with digital force transducers (Columbus Instruments, Columbus, OH, USA). For forepaw measurements mice were suspended by the tail and allowed to grasp the pull bar. Once both paws were secured the mouse was pulled back along a straight line, by the tail, until it released its grip and maximum force was attained. For the hind paw measurement, mice were allowed to grasps a grip grid held by testers right hand to stabilized the forepaws, tail was grasped by the left hand and mouse's hind paws were placed on the push bar. Once both paws were secure, the mouse was pulled back towards transducer in one fluid motion by tester and maximal force was obtained. Six consecutives measurements were recorded alternating between the fore and hind paws, such that there were 3 recordings per paw for each mouse. Data was plotted as an average of 3 trials for each paw.

Blood sampling and plasma separation

To measure NFL levels in the mice, blood was collected via cardiac puncture. Blood was collected in K2 EDTA

Micro500 tubes (part# M500-E, SAI Infusion Technologies, Lake Villa, IL, USA), stored on ice until all samples were collected and then spun down at 4 °C for 3 min at maximum speed. The plasma was pipetted into clean tubes and immediately frozen at −80 °C until processed.

Measurement of NFL in plasma

In vivo plasma concentration of NFL was measured using the Simoa NF-Light Advantage Kit (#103186) at Quanterix, Inc, Billerica, MA, USA. The Simoa assay is a 2-step digital immunoassay, which measures the quantity of NfL in samples using the Simao HD-1 Analyzer and Single Molecule Array (Simoa) technology.

Tissue harvest and processing for immunohistochemistry

Mice were euthanized using 2.5% tribromoethanol (0.5 ml/25 g body weight) and transcardially exsanguinated with phosphate-buffered saline (PBS). Brain, spinal cord and sciatic nerve were dissected, weighed, placed on dry ice to freeze and stored at −80 °C until processed. For tissues collected for histology PBS perfusion was followed by 4% paraformaldehyde (PFA) perfusion for fixation. Spinal cords were dissected and post-fixed overnight in 4% PFA, then transferred into PBS and shipped to NeuroScience Associates, Knoxville, TN, USA for sectioning and histology. Sciatic nerve was harvested 2 to 3 cm proximal to the branch of the tibial, peroneal and sural nerves and post-fixed for 24–48 h in Karnovsky's solution (2% PFA, 2.5% Glutaraldehyde, in 0.1 M Cacodylate Buffer pH 7.35) and then transferred to the pathology department for sectioning and histology.

Immunohistochemistry in mouse spinal cord and sciatic nerve

Lumbar spinal cords were sectioned and stained as described in [42]. Tissues were multiply embedded into a gelatin matrix using MultiBrain Technology (NeuroScience Associates) and each MultiBrain block was sectioned coronally at 25 µm. A series of 33 sections, equally spaced at 300 mm intervals throughout the entire lumbar cord was used for staining. IHC staining was performed using goat anti-ChAT (choline acetyltransferase; Millipore #AB144P, AB_2079751) and rabbit anti-Iba1 (Wako #019-19741, AB_839504), rat anti-CD68 (Bio-Rad #MCA1957T, AB_2074849) counterstained with Nissl (0.05% thionine/0.08 M acetate buffer, pH 4.5, Amino cupric silver (de Olmos Stain) and rabbit anti-dMBP (Millipore #AB5864, AB_2140351).

Whole slide imaging for spinal cord was performed at 200X magnification using the Nanozoomer (Hamamatsu Corp, San Jose, CA, USA) system. 10–12 images per mouse in the L3-5 regions were analyzed using Matlab (Mathworks, Natick, MA, USA). Tissue sections, motor neurons, microglia, and degeneration stains were detected using color thresholds and morphological operations. A regional minima and radial symmetry detection [43] with watershed segmentation followed by morphological, shape and size filtering were used to further enumerate DAB positive cells. Image analysis was performed blinded to experimental grouping and genotype.

For PPD staining, sciatic nerves were washed in 0.1 M Sorensen's buffer (Electron Microscopy Sciences, Hatfield, PA, USA #11600-10), post-fixed with agitation in 1% osmium tetroxide (Electron Microscopy Sciences #19150) in 0.1 M Sorensen's buffer for 24 h at 4 °C and washed in 0.1 M Sorensen's buffer. Nerves were incubated en bloc in 2% uranyl acetate (Ted Pella, Redding, CA, USA #19481) for 1 h and washed again in 0.1 M Sorensen'd buffer. Sciatic nerves were dehydrated with agitation in 70%, 95%, and 100% 200 proof ethanol (Sigma-Aldrich #459844) twice for 10 min each, and in propylene oxide (Ted Pella #18601) twice for 10 min each. The nerves were then infiltrated with eponate 12 resin (Ted Pella #18005) with agitation as follows: 1:1 Epnate/propylene oxide for 12 h, 2:1 eponate/propylene oxide for 4 h, and pure eponate for 4 h. The nerves were embedded in eponate in flat silicone embedding molds and polymerized at 70 °C overnight. Blocks were sectioned on an automated ultramicrotome (Leica EMUC7) set to cut 1 µm thick sections. Sections were collected on Superfrost positively charged glass slides (Thermo Scientific). Slides were stained with 2% p-phenylenediamine (Sigma-Aldrich #78429) in 50% ethanol for 10–15 min, rinsed in water for 10 min, air dried, and coverslipped with Cytoseal 60 (Thermo Scientific #MMC0343).

For CD68 immunohistochemistry on the sciatic nerves, nerves were formalin fixed, processed, and embedded longitudinally in paraffin. CD68 immunohistochemistry was performed with the Abcam anti-CD68 rabbit polyclonal antibody (Abcam #AB125212, AB_10975465) at 0.25 µg/ml on the Ventana Discovery XT platform with CC1 standard retrieval and OmniMap detection with DAB chromogen and hematoxylin counterstain. Normal mouse lung, liver, and kidney were used as positive controls.

Whole slide imaging for sciatic nerve was performed at 400X magnification using the Nanozoomer system at a resolution of 0.23 µm/pixel. Region of interest (ROI) outlining the cross sectional area of the nerve were manually drawn and analyzed at full resolution using Matlab. The images were converted to gray scale and initial segmentation of lumen and myelin area was determined using

intensity thresholding and rolling-ball filtering. Additional segmentation was performed by applying the Laplace operator on Gaussian smoothed images, and by morphological and HSI (hue, saturation, intensity) processing within watershed separated regions. Detected objects were further selected based on morphological reconstruction, mean intensity, size and shape factor analysis. Average lumen size was calculated by summing the total lumen area within myelinated axons and dividing that by the total number of myelinated axons that contains a lumen. Total myelin area of axons that contained a lumen was normalized to the ROI area. The number of collapsed axons that did not have obvious cytoplasmic lumens were manually counted. All analysis was performed in a blinded manner.

Gene expression analysis

Lumbar spinal cords from 18-week-old mice were homogenized using soft tissue homogenization tubes (OMNI #19-627). RNA was extracted using RNeasy Mini Kit according to manufacturer's instructions (Qiagen #74104). RNA concentration and quality were analyzed by NanoDrop 8000 or Agilent 2100 Bioanalyzer in combination with RNA Pico Chips. 100–300 ng total RNA was hybridized with reporter and capture probes for nCounter mouse neuroinflammation code set and analyzed according to manufacturer's instructions (nSolver analysis system, Nanostring, Seattle, WA, USA). For normalization, expression levels of housekeeping genes *Gapdh*, *Pgk1* and *Tubb5* were used.

Immunohistochemitry for human samples – tissue procurement, ethics statement, fixation, antibodies, generation of positive controls

Human samples for IHC were procured with a clinical diagnosis of ALS or normal (no associated neurologic disease) from commercial sources under warranty that appropriate Institutional Review Board approval and informed consent were obtained. All studies with human tissue were approved by Genentech Human Tissue Lab review committee. All tissues were formalin fixed and paraffin embedded. pRIP1 immunohistochemistry was performed with the rabbit monoclonal antibody D1L3S (Cell Signaling Technology, AB_2799693) at 0.5 µg/ml on the Ventana Benchmark platform with CC1 standard retrieval, Ventana Discovery goat Ig Block, and Optiview Amplification with DAB and hematoxylin counterstain. Total RIP1 was detected with the Lifespan Biosciences mouse monoclonal antibody 7H10 (AB_1540216) that was used at 0.5 µg/ml. Immunohistochemistry was performed on the Dako platform with Target retrieval, and hydrogen peroxide and BSA block. The reaction was detected with PowerVision polymer HRP detection with DAB and hematoxylin counterstain. HT-29 cells with and without TNF/BV6/zVAD treatment were used as controls for pRIP1 immunohistochemistry. Wild-type and KD RIP1 HT-29 cells with and without TNF/BV6/zVAD treatment were used as controls for pRIP1 immunohistochemistry. To test phosphospecificity of the pRIP1 antibody, slides of HT29 cell pellets were treated with lambda phosphatase prior to immunolabeling to confirm that loss of phopho-residues abrogated all labeling. Primary antibodies were replaced with isotype matched antibodies as a reaction negative control.

MPTP model in mice

MPTP was administered to male C57Bl/6N mice (Psychogenics, Paramus, NJ, USA) once daily for 5 days in a dose-ranging study (15, 20 and 25 mg/kg) to determine the MPTP dose that would produce ~50% reduction in striatal levels of the neurotransmitter dopamine. Following 7 days post-onset of MPTP treatment, animals were euthanized via decapitation and left and right striata were individually weighed and collected on dry ice into 2 ml conical tubes (Sarstedt, Sparks, NV, USA #72.693) for measurements of the neurotransmitter dopamine and its metabolites. These measurements were carried out independently for both sides of the striata and averaged per animal.

To test the efficacy of the genetic depletion of RIP1 kinase activity, wild-type and RIP1-KD mice were treated with 17.5 mg/kg MPTP (or saline vehicle) as described above. Following 7 days post-onset of MPTP treatment, animals were euthanized via decapitation and dissected brains were placed in a RBMA-200C Kent 1 mm matrix brain block to separate the frontal area from the rest of the brain. The front part of the brain was divided into 2 hemispheres, leaving the posterior as one intact piece. Left striatum was dissected out, collected on dry ice, and stored at −80 °C until the analysis of the dopamine levels. The right-front and the rest of the brain were post-fixed in 4% PFA for 48 h, transferred to PBS with 0.01% sodium azide for analysis of TH staining by immunohistochemistry.

Measurement of dopamine, DOPAC and HVA

The content of dopamine, DOPAC and HVA were measured in striatal lysates by HPLC with electrochemical detection (HTEC-500, Eicom Corp., Kyoto, Japan). Samples were injected using a CMA/200 Refrigerated Microsampler (CMA/Microdialysis). Dopamine, DOPAC, and HVA were separated on a 150 × 2.1 I.D. mm column (CA5-ODS) with the mobile phase consisting of 0.1 M phosphate buffer at pH 6.0, 0.13 mM EDTA, 2.3 mM sodium-1-octanesulfonate and 20% methanol. The chromatograms

were recorded and integrated by use of a computerized data acquisition system (DataApex, Prague, The Czech Republic).

Immunohistochemistry for TH in MPTP-treated mice

Immunohistochemistry for TH was performed with a rabbit polyclonal antibody (Millipore #AB152, AB_390204) at 2.5 µg/ml on the Ventana Discovery XT platform with CC2 mild antigen retrieval, BSA block, and OmniMap detection with DAB and hematoxylin counterstain. Mouse brain was used as a positive control.

Statistics

No statistical methods were used to pre-determine sample sizes. The number of animals used in the experiments were similar to previous studies in the SOD1-Tg model [40]. In SOD1-Tg experiments, animals of different genotypes were caged together. In MPTP experiments, wild-type mice were randomized to different treatment groups. Genotypes were not available to the experimenter during data acquisition or analysis. Image analysis on the animal studies and immunochemistry in human tissue were performed in a blinded fashion. Immunohistochemistry sections with high background signal were excluded in the final analysis. Exclusion was performed blinded to the genotype or treatment. No other data were excluded in the study. Normal distribution was assessed by the Kolmogorov–Smirnov test. Homogeneity of variance was assessed by Bartlett's Test in groups that are being compared by parametric One-Way ANOVA tests. Comparisons between two groups were performed by Mann–Whitney test. For multiple group comparisons, the following tests were used: Non-parametric Kruskal–Wallis One-Way ANOVA test with Dunn's multiple comparison post-hoc test, parametric Brown-Forsythe and Welch One-Way ANOVA with Dunnett's T3 multiple comparison post-hoc test, and Two-Way ANOVA with Tukey multiple comparison post-hoc test. p values were represented as $*p < 0.05$, $**p < 0.01$, and $***p < 0.001$. All error bars denote standard error of the mean (S.E.M.). GraphPad v8 was used to compute the statistical parameters.

Results

RIP1 protein levels are upregulated in late-stage disease without detectable RIP3 or MLKL in the SOD1-Tg mice

We first examined whether disease progression in the SOD1-Tg mice is correlated with changes in markers of the necroptosis pathway by immunoblotting in lumbar spinal cords of ~8-, ~12- and ~16-week-old SOD1-Tg mice. We immunoblotted spinal cord lysates for RIP1 with a validated antibody that produced a signal in wild-type but not in the RIP1 KO mouse embryonic fibroblasts (MEFs) (Supplementary Fig. 1A). The total protein level of RIP1 in the lumbar region of spinal cords was increased by ~30% in ~16-week-old SOD1-Tg mice as compared to wild-type animals, without a significant difference between the two genotypes in younger animals (Fig. 1a, b, RIP1/Tubulin). Similar results were obtained when RIP1 immunoblot signal was normalized to GAPDH (Supplementary Fig. 1B). In contrast, RIP1 protein amount in the cortex and sciatic nerve were similar between the genotypes at all ages (Supplementary Fig. 1C–E), though SOD1-Tg sciatic nerves had a trend of increased RIP1 at 8-weeks of age (Supplementary Fig. 1C, E). We next measured autophosphorylation of RIP1 on S166, a marker of RIP1 kinase activation [3–5]. In control experiments, stimulation of a mouse cell line, L929, with a necroptosis-inducing cocktail (TBZ) induced the expected pRIP1(S166)-immunoblot signal in anti-RIP1 immunoprecipitates (IPs, Supplementary Fig. 1F). In contrast, pRIP1(S166) was not detected in RIP1 IPs from extracts of 14-week-old SOD1-Tg brain or spinal cords (Supplementary Fig. 1F). Thus, RIP1 activation was not detectable in the SOD1-Tg spinal cords despite the ongoing motor neuron degeneration.

We next examined protein levels of RIP3 and MLKL in SOD1-Tg spinal cords. We first tested the specificity of anti-RIP3 and -MLKL antibodies used in previous studies [25, 36] and a custom anti-RIP3 antibody (GNE 1G6.1.4 [38]) in immunoblots with the corresponding *Rip3* or *Mlkl* KO MEF lysates. Among the four antibodies tested against RIP3 or MLKL, only the anti-RIP3 GNE 1G6.1.4 antibody and two anti-MLKL antibodies (SAB1302339, MABC604) produced specific immunoblot signal of their respective targets (Supplementary Fig. 1G, H). Others were either not specific or did not produce a signal. Immunoblots in lysates from HT-29 cells treated with *Rip3* or *Mlkl* siRNAs highlighted additional antibodies that are suitable for immunoblotting in human cells (Supplementary Fig. 1G, H). Thus, we used the anti-RIP3 (GNE 1G6.1.4) and anti-MLKL (MABC604) antibodies to test RIP pathway activation. Consistent with previous publications [29, 36], we were unable to identify RIP3 or MLKL immunoblot signal in the spinal cords in either wild-type or SOD1-Tg mice, despite strong and specific signal in wild-type MEFs (Fig. 1c, d). Further immunoblotting experiments in wild-type mice confirmed RIP1 expression in all brain regions and peripheral organs, whereas RIP3 and MLKL expression were limited to the latter (Fig. 1e, Supplementary Fig. 1I).

Together, these data indicate a potential induction of RIP1 protein in the late-stage disease without a strong

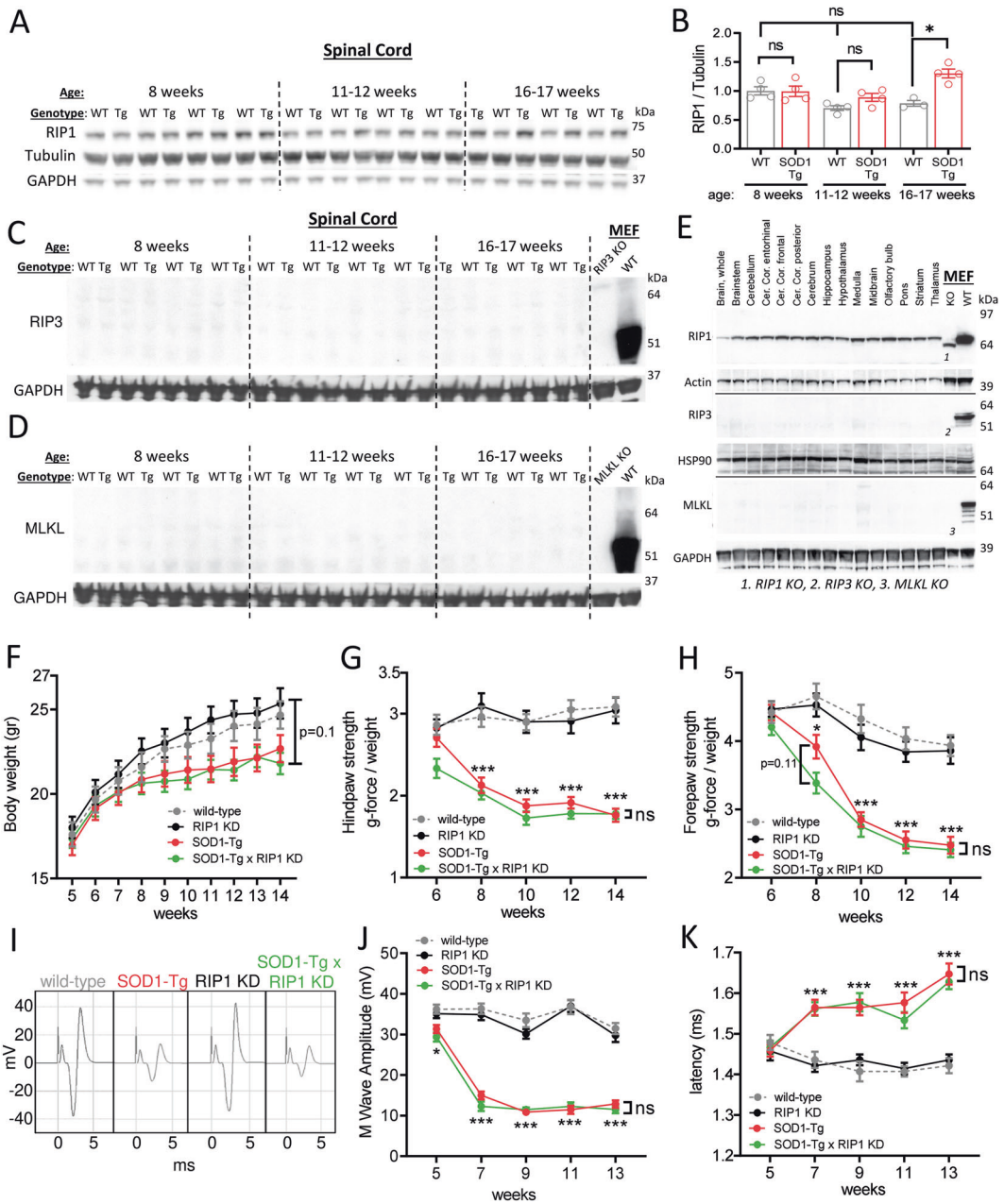

Fig. 1 Increased pRIP1 in SOD1-Tg mice spinal cords in late-stage disease without detectable expression of RIP3 or MLKL. Genetic inactivation of RIP1 kinase does not provide protection against declining muscle strength and nerve physiology in the SOD1-Tg mice. (**a**) Immunoblotting for RIP1, Tubulin and GAPDH in lysates from lumbar region of the spinal cords of WT and SOD1-Tg animals at the indicated ages. (**b**) Quantification of the immunoblot signal for RIP1 normalized to Tubulin, from (**a**). $*p < 0.05$ by One-Way ANOVA (Dunn's). $n = 3, 4$ mice/age/genotype. **(c, d)** Immunoblotting for RIP3 (**c**) and MLKL (**d**) in lysates from lumbar region of the spinal cords of WT and SOD1-Tg animals at the indicated ages. WT and KO MEFs were used to verify the specificity of the immunoblotting signal as indicated. **(e)** Immunoblotting for the indicated proteins in lysates of brain regions in wild-type mice. In addition, lysates of wild-type MEFs and the corresponding RIP1, RIP3 or MLKL KO MEFs are immunoblotted to validate the immunoblotting antibodies. **(f)** Body weights of the mice with the indicated genotypes and ages. $n = 14$-18 animals/genotype. $p = 0.1$ by Two-Way ANOVA. **(g, h)** Hindpaw (**g**) and Forepaw (**h**) grip strength of mice with the indicated genotypes and ages. $n = 14$-18 animals/genotype. $*p < 0.05$ and $***p < 0.001$ by Two-Way ANOVA (Tukey) between wild-type and SOD1-Tgs. **(i)** Representative CMAP traces recorded at the Tibialis Anterior Muscle of the mice with the indicated genotypes and ages. **(j, k)** Quantification of M Wave amplitude (**j**) and latency (**k**) in CMAP measurements, from (**i**). Wave amplitude and latency reflect the number of functional axons and speed of conductance, respectively. $n = 14$-18 animals/genotype. $*p < 0.05$ and $***p < 0.001$ by Two-Way ANOVA (Tukey) between wild-type and SOD1-Tgs. All error bars represent S.E.M.

evidence for necroptosis pathway activation in the SOD1-Tg mice.

Genetic inactivation of RIP1 kinase does not modify disease course in the SOD1-Tg mice

To further investigate the role of RIP1 kinase activity in the pathogenesis of SOD1-Tg mice, we examined disease progression in SOD1-Tg x RIP1-KD mice with functional endpoints from 5-weeks of age up to 14-weeks of age. SOD1-Tg mice had slower weight gain, and displayed a progressive decline in grip strength in both hind and fore-paws starting at 8-weeks of age (Fig. 1f–h), reflecting the onset of muscle denervation. Compared to SOD1-Tgs, SOD1-Tg x RIP1-KD animals similarly had slower weight gain (Fig. 1f) and displayed reduced grip strength (Fig. 1g, h). The lack of RIP1 KD effect was persistent when data were analyzed separately for males and females (Supplementary Fig. 1J–M). In addition, compound muscle action potential (CMAP) recorded at the Tibialis Anterior Muscle showed progressively deteriorating nerve conduction in both SOD1-Tg and SOD1-Tg x RIP1-KD animals (Fig. 1i–k). Thus, genetic inactivation of RIP1 kinase does not provide protection against declining muscle strength and nerve physiology in the SOD1-Tg mice.

Genetic inactivation of RIP1 kinase does not alter axonal pathology and neurodegeneration in the SOD1-Tg mice

We next performed immunohistochemical analysis in 14-week-old mice since SOD1-Tgs have ongoing neurodegeneration at this time point prior to the onset of the end-stage disease [40]. We performed immunohistochemical analysis of axonal integrity in the sciatic nerve by staining myelin with paraphenylenediamine (PPD). In the SOD1-Tgs, sciatic nerve axons on average had smaller lumen areas (Fig. 2a, b) with an overall reduction in the myelin staining across the nerve (Fig. 2a, c). In addition, SOD1-Tg sciatic nerves occasionally had axons without obvious cytoplasmic lumens, hereby referred to as “collapsed axons” (asterisks in Fig. 2a, d). Inactivation of RIP1 kinase in the SOD1-Tgs did not alter these markers of nerve degeneration in the SOD1-Tg x RIP1-KD sciatic nerves (Fig. 2a–d). In addition, we observed infiltration of CD68-positive cells in the sciatic nerves of SOD1-Tgs to a similar level as in the SOD1-Tg x RIP1-KD animals (Fig. 2a, e).

In the spinal cord, SOD1-Tgs had motor neuron degeneration as evidenced by ~40% reduction in the number of Choline Acetyltransferase (CHAT)-positive cells (Fig. 3a, b). Further highlighting neurodegeneration, PPD staining indicated an increased number of collapsed axons (Fig. 3a, c), and amino-cupric-silver staining (A-Cu-Ag, De [44]) confirmed degenerating neurites and cell bodies in SOD1-Tgs (Fig. 3a, d). We did not observe a benefit of inactivation of RIP1 kinase activity in any of these neurodegeneration-related endpoints (Fig. 3a–d). In addition, we stained for degraded myelin basic protein (dMBP) in the SOD1-Tg spinal cords as an approximate measure of demyelination [45]. In SOD1-Tgs, we detected accumulation of dMBP, consistent with previous studies demonstrating oligodendrocyte dysfunction and demyelination in this model [25, 46, 47]. SOD1-Tg x RIP1-KDs accumulated similar levels of dMBP compared to SOD1-Tgs, confirming that the kinase activity of RIP1 does not significantly contribute to pathology in the SOD1-Tg spinal cord (Fig. 3a, e).

Since SOD1-Tg animals display progressive neurodegeneration, we examined if RIP1 kinase inactivation alters neurodegeneration in a longitudinal cohort by measuring the plasma levels of neuronal injury marker Neurofilament L (NfL). NfL is an axonal protein that is released from stressed or degenerating neurons, and accumulates in the plasma and CSF of animal models and patients of neurodegenerative disorders [48]. In SOD1-Tg animals, plasma NfL levels displayed three phases: First, a ~3-fold increase between the ages of 8- and 12-weeks, followed by stable levels (but remain elevated) between the ages of 12- and 14-weeks, followed by a further ~2-fold increase between the ages of 14- and 18-weeks (Fig. 3f). These two bouts of increase in plasma NfL levels likely reflect the initial denervation and the subsequent motor-neuron cell-body degeneration observed in the SOD1-Tg mouse. Consistent with a lack of RIP1 kinase effect on neurodegeneration, plasma NfL levels in SOD1-Tg x RIP1-KD animals followed a similar time course to SOD1-Tgs across all ages (Fig. 3f).

Genetic inactivation of RIP1 kinase does not alter inflammation in the SOD1-Tg mice

Lastly, we examined the markers of inflammation in the spinal cord of SOD1-Tg mice. Coincident with neurodegeneration, SOD1-Tg mice had increased Iba1-positive staining in the spinal cord, indicating a microgliosis response (Fig. 4a, b). SOD1-Tg x RIP1-KD mice had similar levels of Iba1-positive signal compared to the SOD1-Tg animals (Fig. 4a, b). In addition, gene expression analysis in spinal cords measuring 262 neuroinflammation and 5 RIP pathway-associated mRNAs identified 20 downregulated and 49 upregulated genes in the SOD1-Tg mice compared to the wild-type mice (Fig. 4c, d). *Chat* and *Mbp* genes were among the downregulated genes, highlighting the neurodegeneration and demyelination in this model. Pathway analysis indicated that the most significantly upregulated genes belonged to the IL10-signaling and complement pathways (Supplementary Fig. 2A).

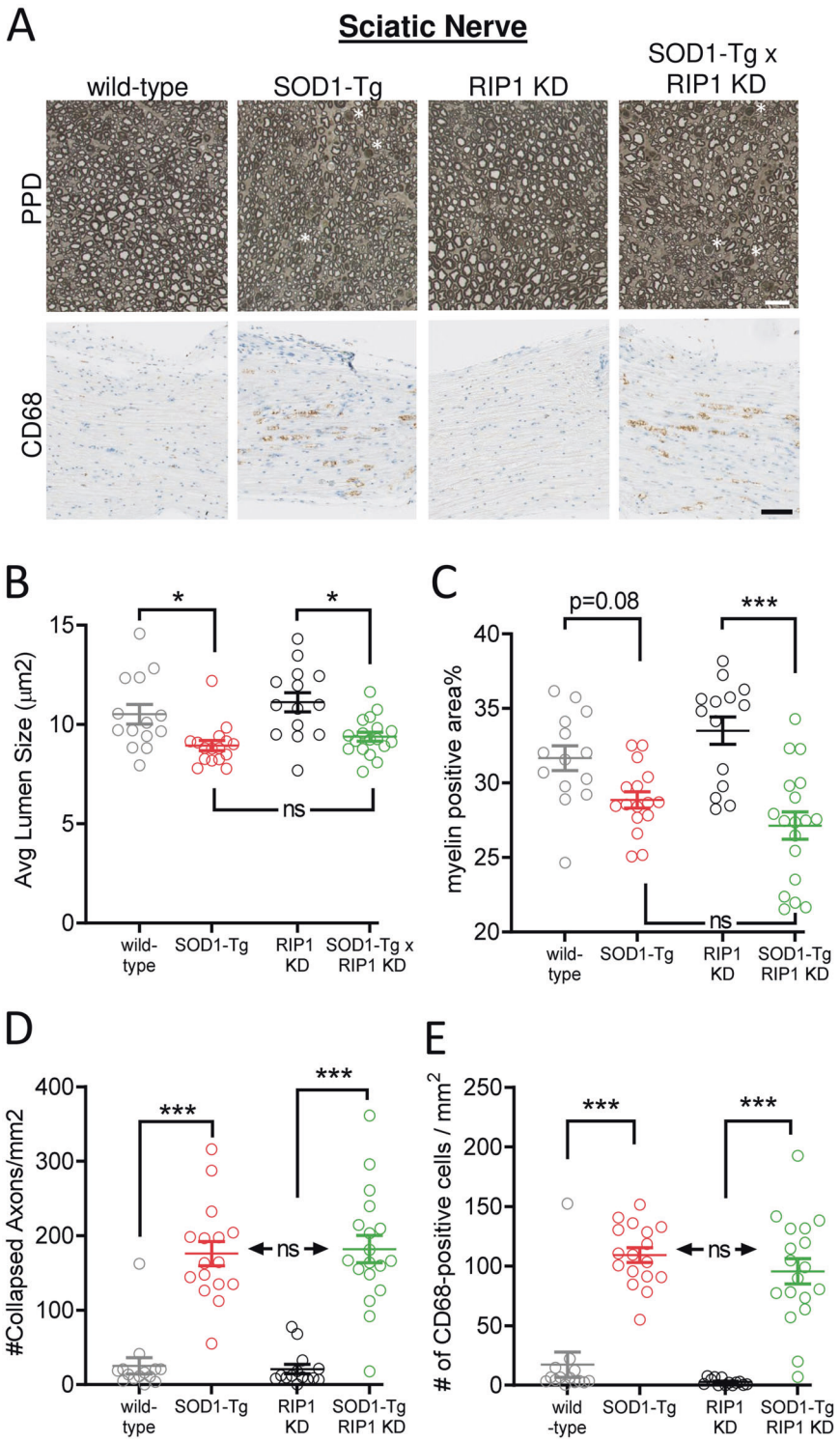

Fig. 2 Genetic inactivation of RIP1 kinase activity does not alter axonal pathology in the SOD1-Tg mice. (**a**) PPD and anti-CD68 staining in sciatic nerves of 14-week-old mice with the indicated genotypes. Scale bars, 10 µm for PPD staining and 90 µm for anti-CD68 staining. **(b-d)** Quantification of lumen size (**b**), myelin-positive area (**c**), and number of collapsed axons per mm^2 (**d**) calculated based on PPD staining in (**a**). n = 14-18 animals/genotype. *$p < 0.05$ and ***$p < 0.001$ by One-Way ANOVA (Dunn's). **(e)** Quantification of number of CD68-positive cells per mm^2, from (**a**). n = 14-18 animals/genotype. ***$p < 0.001$ by One-Way ANOVA (Dunn's). All error bars represent S.E.M.

Rip1 was among the significantly upregulated genes consistent with increased protein abundance of RIP1 in the late-stages of the disease (Fig. 4c, d, Fig. 1a). Interestingly, *Mlkl* mRNA was readily detectable and displayed a trend of increased expression in both SOD1-Tgs and SOD1-Tg x RIP1-KDs (Supplementary Fig. 2B). *Rip3* mRNA was barely detectable across all genotypes (Supplementary Fig. 2B). Importantly, genes that had differential abundance in SOD1-Tgs (Fig. 4d, *x*-axis) were equally up- or down-regulated in the SOD1-Tg x RIP1-KD animals (Fig. 4d, *y*-axis). These data indicate the inflammatory gene expression in SOD1-Tgs is not dependent on RIP1 kinase activity.

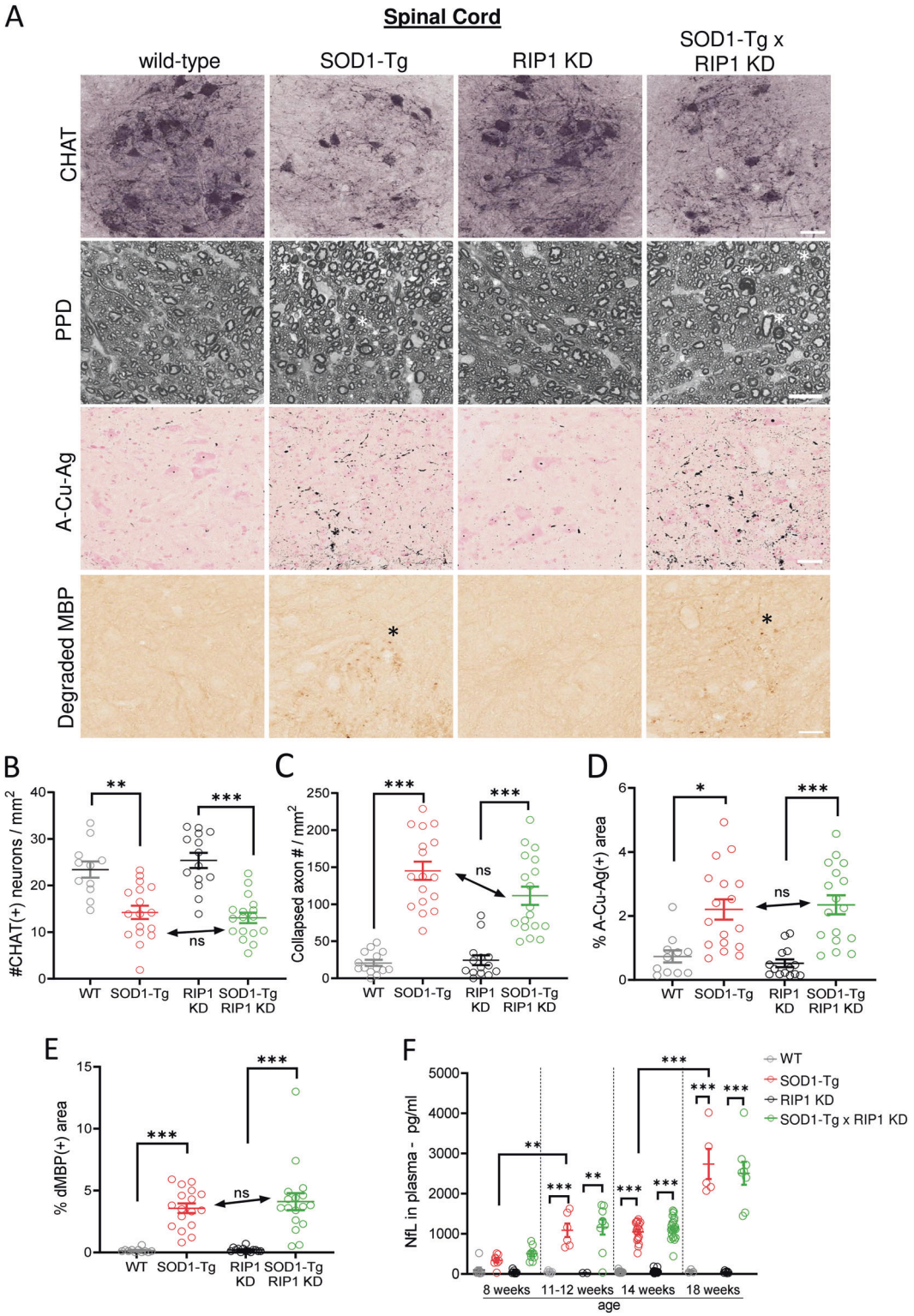

Fig. 3 Genetic inactivation of RIP1 kinase activity does not ameliorate neurodegeneration in the SOD1-Tg mice. (**a**) Anti-CHAT, PPD, A-Cu-Ag and anti-degraded MBP staining in spinal cords of 14-week-old mice with the indicated genotypes. Scale bars: 27 μm for PPD staining and 40 μm for anti-CHAT, A-Cu-Ag and anti-degraded MBP staining. **(b-e)** Quantification of number of CHAT-positive neurons per mm^2 (**b**), number of collapsed axons per mm^2 (**c**), percent A-Cu-Ag (**d**) and degraded MBP (**e**) -positive area in ventral horn of lumbar spinal cord, from (**a**). (**b-d**) were calculated across the entire cross section of L3-L5 spinal cord. $n = 11$-18 animals/genotype. $^*p < 0.05$, $^{**}p < 0.01$ and $^{***}p < 0.001$ by One-Way ANOVA (Dunn's). **(f)** NfL levels in plasma of mice with the indicated ages and genotypes. $n = 2$-23 animals/genotype/age. $^{**}p < 0.01$ and $^{***}p < 0.001$ by Two-Way ANOVA (Tukey). All error bars represent S.E.M.

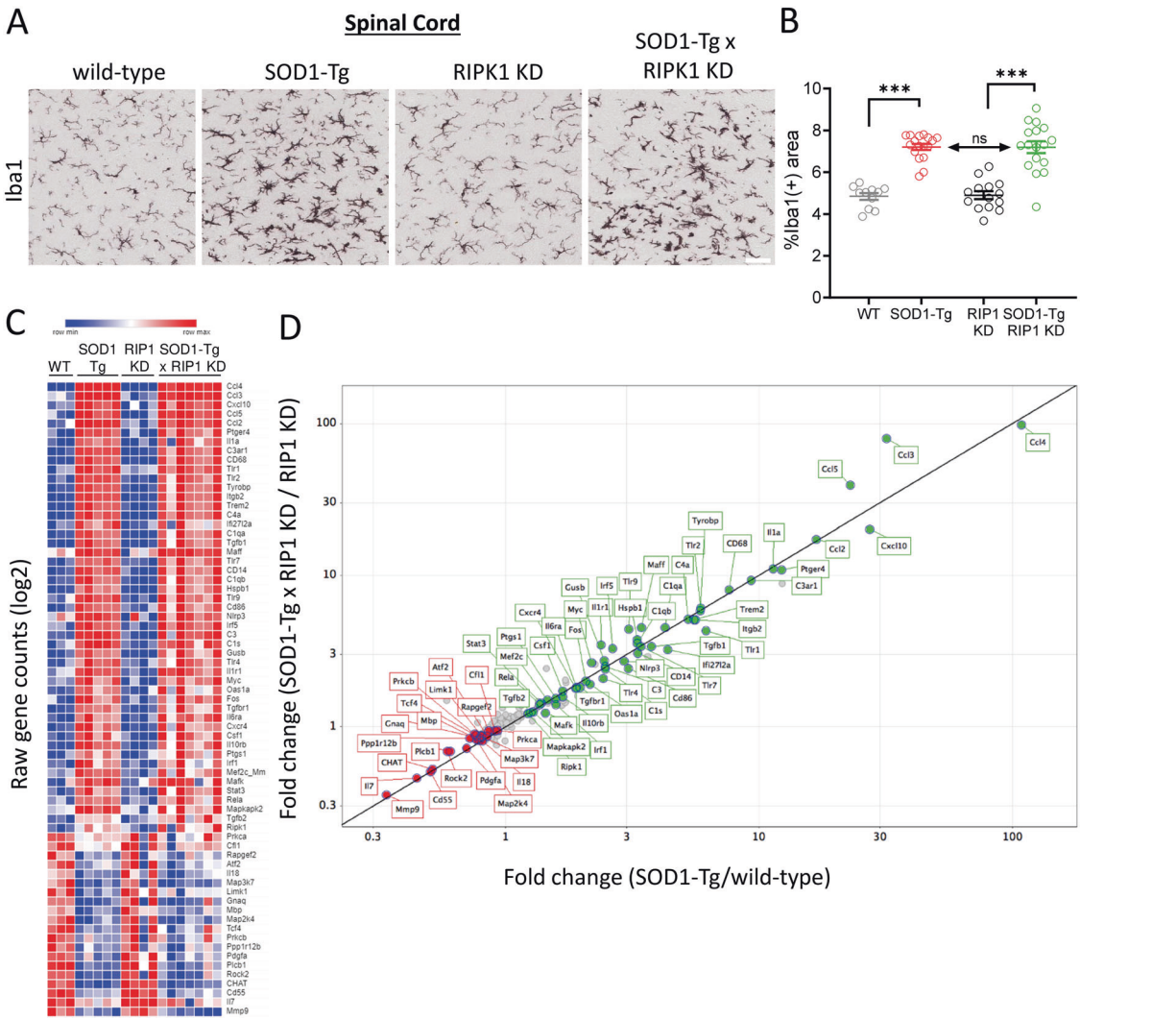

Fig. 4 Genetic inactivation of RIP1 kinase activity does not alter inflammation in the SOD1-Tg mice spinal cords. (**a**) Anti-Iba1 staining in spinal cords of 14-week-old mice with the indicated genotypes. Scale bar, 40 µm. (**b**) Quantification of percent of anti-Iba1-positive area, from (**a**). $n = 11$-17 animals/genotype. $^{***}p < 0.001$ by One-Way ANOVA (Dunn's). (**c**) Heat map depicting gene counts measured by Nanostring analysis in spinal cords of 18-week-old mice with the indicated genotypes. Out of 262 neuroinflammation and 5 RIP pathway-associated mRNAs analyzed, 172 of them showed detectable expression (as defined by >10 counts). Each row represents a gene that displayed differential expression in SOD1-Tgs compared to wild-types among these 172 genes (FDR (Q) < 0.01). Color scale is adjusted within each row based on the highest (red) and lowest (blue) expression of a given gene across all animals. $n = 3$-7 mice. (**d**) Plot showing fold-changes in expression of genes highlighted in (C) between "wild-type vs SOD1-Tgs" (x-axis) and "RIP1-KD vs SOD1-Tg x RIP1-KDs" (y-axis) comparisons. Green symbols: upregulated, red: downregulated, gray: no change $n = 3$-7 mice. All error bars represent S.E.M.

RIP1 kinase activation in ALS is limited to endothelial cells in the spinal nerve without detectable activation in the spinal cord

Since mutations in SOD1 are rare causes of ALS [49], we next sought evidence of RIP1 kinase activation in sporadic disease by staining for pRIP1(S166) in spinal nerve and spinal cord samples from ALS patients. The staining protocol for pRIP1(S166) was validated in HT-29 cells, which showed an induction of signal upon TBZ-treatment (Supplementary Fig. 3A). Furthermore, the TBZ-induced pRIP1 (S166)-signal was erased by phosphatase treatment, and was not observed in RIP1(K45A) kinase-dead cells (Supplementary Fig. 3B). Using the same staining protocol, we next examined spinal nerves and spinal cords from healthy and ALS individuals (Supplementary Table 1). In the spinal nerves, positive pRIP1(S166)-staining was present in higher proportion in ALS samples compared to healthy controls, though a small fraction of healthy samples was also positive (5/7 in ALS vs 2/10 in healthy controls, Fig. 5a). The morphological features of the positive cells were most consistent with vascular endothelium labeling associated

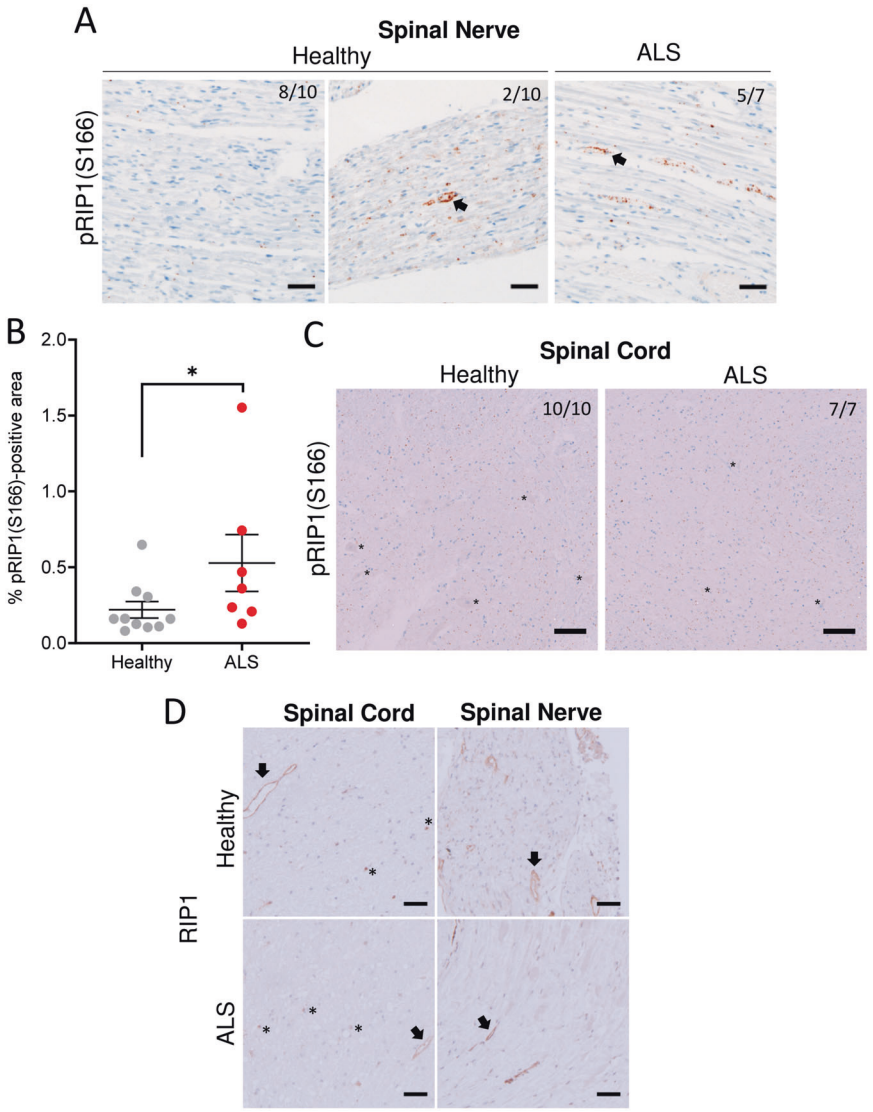

Fig. 5 RIP1 kinase activation in ALS is limited to endothelial cells in the spinal nerve. (a, c) Representative images of pRIP1 (S166) in spinal nerves (**a**) and spinal cords (**c**) of healthy controls and ALS patients. Numbers of samples with the indicated representative staining out of the total number of samples analyzed are indicated at the top of the images. In (**a**), arrows indicate positive-labeling associated with vascular endothelium. In (**c**), asterisks indicate the motor neuron cell bodies. Scale bars, 50 µm. **(b)** Quantification of percent pRIP1 (S166)-positive area in spinal nerves, from (**a**). $n = 7$-10 samples. $^*p < 0.05$ by Mann-Whitney test. **(d)** Representative images of total RIP1 in the spinal cords and nerves. Arrows indicate the positive-labeling associated with vascular endothelium. Asterisks indicate the positive-labeling associated with neuroparenchyma. Scale bars, 50 µm. All error bars represent S.E.M.

with the nerves (Fig. 5a, arrows). Quantification of the percent tissue area positive for pRIP1(S166) confirmed the increase in pRIP1(S166) in ALS spinal nerves (Fig. 5b). Furthermore, post-mortem interval of tissue collection did not correlate with the extent of positive pRIP1(S166) staining (Supplementary Fig. 3C), suggesting the labeling was not an artifact of post-mortem handling and fixation conditions.

In contrast to the spinal nerves, we did not observe pRIP1(S166) in any of the spinal cords from healthy or ALS samples (10 and 7 cases, respectively, Fig. 5c). Note, spinal cord samples were from the same block of tissue where we had observed positive staining in spinal nerves, suggesting lack of labeling in spinal cords is less likely to be due to antigen loss. Importantly, spinal cord samples did stain positive for RIP1 (total), and as expected, so did spinal nerves (Fig. 5d). The specificity of the RIP1 staining was confirmed by differential labeling between wild-type versus *RIP1* KO HT-29 cells and by positive labeling in ileum samples (Supplementary Fig. 3D). In the spinal nerves, RIP1 was found primarily in the endothelial cells (Fig. 5d, arrows), consistent with the staining pattern of pRIP1(S166) (Fig. 5a). In the spinal cord, in the addition to the endothelial labeling, low numbers of cells were labeled in neuroparenchyma (Fig. 5d, asterisks). Overall, we did not observe an obvious difference in RIP1 staining between healthy control versus ALS spinal cords or spinal nerves. These data suggest RIP1 is expressed in both the spinal cord and spinal nerves, however, the activation of RIP1 is limited to the latter.

Genetic inactivation of RIP1 kinase protects in the MPTP-model of dopaminergic neurodegeneration

We next sought evidence of RIP1-mediated pathology in another mouse model of neurodegenerative disease. For this

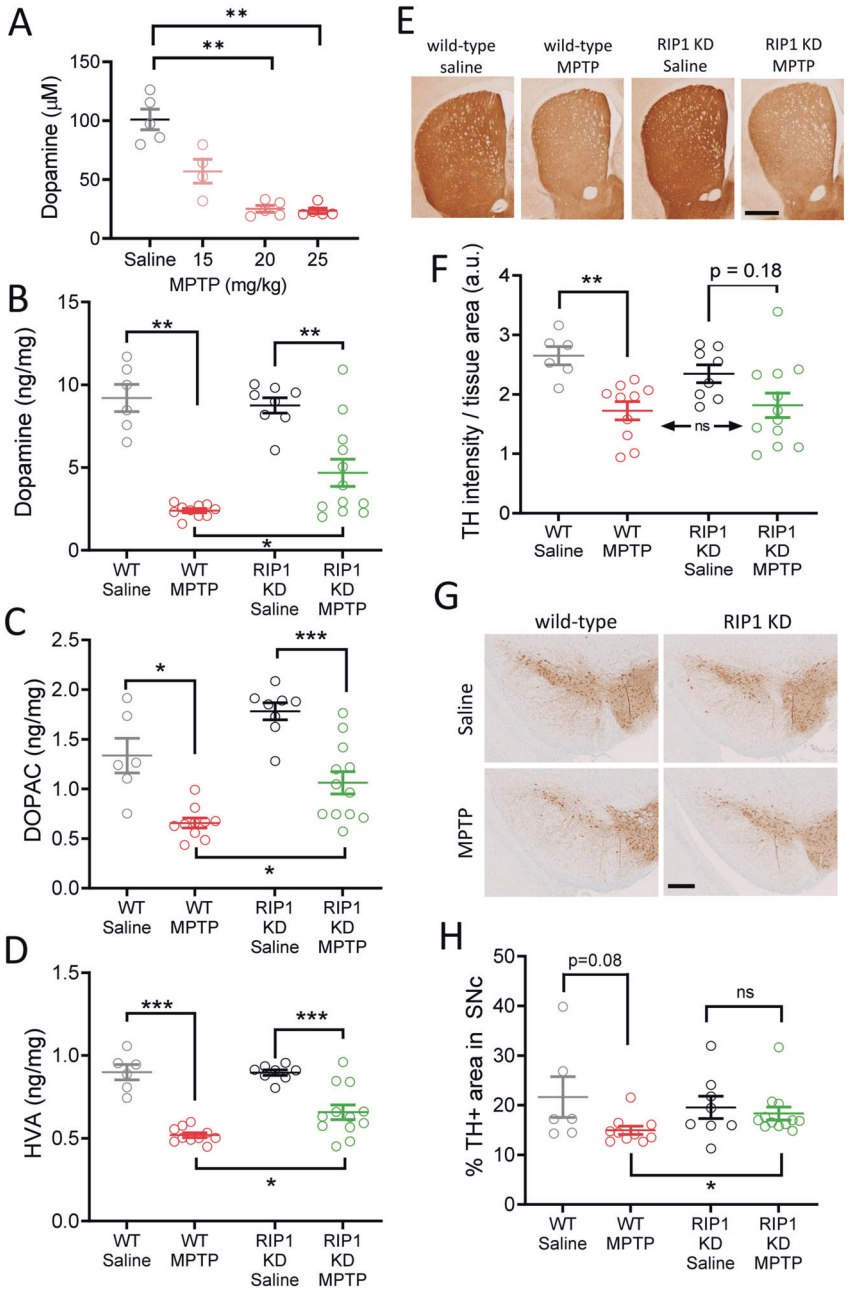

Fig. 6 Genetic inactivation of RIP1 kinase activity is partially protective in the MPTP model. (**a**) Striatal dopamine levels in MPTP-treated wild-type mice. $^{**}p < 0.01$ by One-Way ANOVA (Dunn's). $n = 4$-5 mice/group. **(b-d)** Striatal dopamine (**b**), DOPAC (**c**) and HVA (**d**) levels in Saline or MPTP-treated wild-type and RIP1-KD mice. The analysis was performed at 7 days post-MPTP treatment. $^{*}p < 0.05$, $^{**}p < 0.01$ and $^{***}p < 0.001$ by Brown-Forsythe and Welch One-Way ANOVA (Dunnett's T3). $n = 6$-12 mice/group. **(e, g)** Immunohistochemistry for TH in striatum (**e**) and midbrain (**g**) of Saline or MPTP-treated wild-type or RIP1-KD mice. Scale bars, 700 μm (**e**), 300 μm (**g**). (**f**, **h**) Quantification of striatal TH density (**f**) and percent of TH + area in the substantia nigra, from (**e**) and (**g**), respectively. $^{*}p < 0.05$ and $^{**}p < 0.01$ by One-Way ANOVA (Dunn's). $n = 6$-12 mice/group. All error bars represent S.E.M.

purpose, we focused on the MPTP toxin model of dopaminergic neurodegeneration. MPP^{+} (an MPTP metabolite) is a mitochondrial neurotoxin preferentially taken up by dopaminergic neurons, thus modeling the neurodegeneration and depletion of the neurotransmitter dopamine in Parkinson's Disease [50]. Importantly, pharmacological inhibition of RIP1 [22] and genetic depletion of RIP3 [51, 52] or MLKL [52] have been suggested to ameliorate degeneration of dopaminergic neurons. To further these findings, we treated RIP1-KD mice with MPTP in a sub-acute paradigm. The dose of MPTP was chosen based on a pilot study designed to determine a dosage that would lead to a ~50% loss of striatal dopamine (Fig. 6a). Interestingly, RIP1-KD mice were partially protected from MPTP toxicity, and had ~2x higher levels of striatal dopamine as compared to the MPTP-treated wild-type mice (Fig. 6b). MPTP-treated RIP1-KD mice also had higher levels of dopamine metabolites DOPAC and HVA (Fig. 6c, d).

We next examined the integrity of dopaminergic terminals and cell bodies by staining for tyrosine hydroxylase (TH) in the striatum and substantia nigra, respectively. As expected, MPTP treatment reduced the density of TH staining in the striatum (Fig. 6e, f). Despite the amelioration of dopamine depletion, MPTP-treated RIP1-KD mice had

similar levels of striatal TH immunoreactivity as compared to MPTP-treated wild-type mice (Fig. 6e, f). In the substantia nigra, MPTP treatment caused a trend towards reduced TH staining in wild-type animals (Fig. 6g, h). Interestingly, the RIP1-KD mice had a subtle but significant increase in the level of TH staining in substantia nigra as compared to the wild-type mice (Fig. 6g, h). These data suggest that inhibition of RIP1 kinase activity can benefit the function of surviving dopaminergic neurons without a large impact on the overall extent of neurodegeneration.

Discussion

In this study, we examined the role of kinase activity of RIP1 in driving neurodegeneration and inflammation in the SOD1-Tg mice. We observed increased total protein levels of RIP1 in spinal cords of the late-stage but not early-stage disease, consistent with previous reports [29, 36]. Since RIP1 is expressed in multiple cell types including microglia and astrocytes [53], the increase in RIP1 protein level could simply reflect the ongoing gliosis and the associated changes in the cellularity of the tissue, rather than RIP pathway activation. Consistent with this, and similar to previous studies [29, 36, 54, 55], we did not find evidence for RIP1 (S166) phosphorylation in the SOD1-Tg, or expression of RIP3 and MLKL in wild-type or SOD1-Tg spinal cords. Future studies could focus on expression analysis on single-cell scale to eliminate the caveats with bulk tissue analysis.

Since lack of detectable RIP1 phosphorylation could be explained by a transient signal in dying cells or by a small proportion of cells undergoing necroptosis/inflammation, we further tested the functional importance of RIP1 kinase in promoting pathology in the SOD1-Tg animals. Importantly, previous studies [29, 36] left open the possibility that RIP1 kinase activity could contribute to pathology independent of RIP3/MLKL, similar to other models of tissue injury and inflammation [13, 14, 56–59]. In the SOD1-Tg model, genetic inhibition of RIP1 kinase did not improve any disease phenotypes including motor dysfunction, nerve conduction, axonal pathology, demyelination, motor neuron degeneration, inflammation. In particular, RIP1-KD mice did not show improvement in a longitudinal analysis of NfL accumulation in plasma, which reflects the progressive neuronal injury. Ito et al. showed inhibition of RIP1 kinase with intracerebroventricular administration of Nec1 could benefit the myelin decompaction phenotype in SOD1-Tg spinal cord axons [25]. However, in this study, it was not clear if Nec1 reached the target tissue and engaged the target. In addition, another study did not find a genotype-specific dilated-myelin phenotype in SOD1-Tgs (or in OPTN KOs) and attributed these findings to technical variability in tissue processing [29]. Beyond the axonal phenotype, our results do not support a beneficial role of RIP1 inhibition in the more established degenerative- and inflammation-related pathologies in the SOD1-Tg mice. On the other hand, partial benefit of RIP1-KDs in the MPTP-model suggest RIP1 kinase activity may have utility in acute injury settings in the brain. Consistent with this view, genetic inactivation of RIP1 kinase also improves acute cell death and functional outcomes in the intracerebral hemorrhage model in mice [15].

Importantly, our data do not exclude the utility of RIP1 inhibition in ALS since mutant SOD1 mice do not recapitulate all degenerative and clinical aspects of the sporadic disease [35, 60]. Furthermore, *SOD1* mutations are a rare cause of ALS [49], and *SOD1*-mutation carrying patients do not develop the hallmark TDP43-pathology in sporadic ALS [61]. To this end, we have performed immunohistochemistry studies in ALS to examine activation of the pathway using a pRIP1(S166) antibody validated for its phospho-signal specificity [3–5]. Interestingly, we observed increased positive staining in endothelial cells in the ALS spinal nerves compared to healthy controls. Though the significance of the endothelial pRIP1(S166)-staining for ALS disease is not fully clear, endothelial cell degeneration has been proposed to contribute to motor neuron degeneration in ALS [62–64]. Since RIP1 can drive endothelial cell necroptosis [65–67], future studies could focus on the importance of RIP1 activation in the endothelial compartment in ALS.

Despite the positive signal in the matching spinal nerves, pRIP1(S166) was not detected in any of the healthy or ALS spinal cord samples. Furthermore, Dermentzaki et al. did not identify a difference in total RIP1 protein levels between healthy controls or ALS in motor cortex samples from ALS [29], consistent with the total RIP1 staining shown here. In contrast, Ito et al. reported accumulation of RIP1, RIP3, MLKL and importantly of pRIP1(S14, 15) in spinal cords of the ALS patients by immunoblotting or immunohistochemistry. While the specificity of these immunoassay signals was not verified in Ito et al., it remains possible that pRIP1(S166) may not be a reliable marker of pathway activation in CNS due to the differences in the stability and extent of this phosphorylation site in CNS (versus other tissues). Further studies could also focus on measuring RIP pathway activation in the motor cortex, a degenerating region in ALS not modeled in the SOD1-Tg mice [35].

Ultimately, the data that will answer the importance of RIP1 kinase activity in driving ALS pathogenesis will be in the clinic with safe, potent, and brain-penetrant RIP1 kinase inhibitors. To further inform such studies, RIP1 inhibitors with optimal potency and CNS-accessibility could be employed in additional ALS models that recapitulate inflammation and motor neuron degeneration [60]. Though protection in the RIP1-KD dopaminergic system argues

against compensatory mechanisms that counteract the germline loss of kinase activity, pharmacological inhibition of RIP1 in the SOD1-Tg model may still have value if such compensatory mechanisms were engaged in the spinal cord. To further characterize pathway activation and target engagement during the disease course, specific and sensitive reagents that report pathway activation are also needed. Since active RIP1/RIP3/MLKL complexes could be transient, more stable downstream biomarkers of pathway activation could be investigated in animal models and in ALS CSF or tissues.

Data availability

Raw data and uncropped immunoblots could be accessed at Mendeley Data Archive under https://doi.org/10.17632/nmv7x3ptfj.1.

Acknowledgements We thank Shari Lau, Miriam Baca, Margaret Solon and Adam Johnson for technical help, Kim Newton for scientific discussions, and Ben Torres for management of the mouse colonies.

Author contributions SD, EV, AE, DV, and BB conceived the study. SD, EV, RB, KS, JT, JI, TE conducted the experiments. SD, EV, RB, JT, JI, HN, OF, JDW, and BB analyzed the data. BB wrote the manuscript. All authors reviewed and edited the manuscript.

Compliance with ethical standards

Conflict of interest TE and BB are former and all other authors are current employees of Genentech, Inc.

Publisher's note Springer Nature remains neutral with regard to jurisdictional claims in published maps and institutional affiliations.

References

1. Martens S, Hofmans S, Declercq W, Augustyns K, Vandenabeele P. Inhibitors targeting RIPK1/RIPK3: old and new drugs. Trends Pharmacol Sci. 2020;41:209–24.
2. Degterev A, Ofengeim D, Yuan J. Targeting RIPK1 for the treatment of human diseases. Proc Natl Acad Sci USA. 2019;116:9714–22.
3. Degterev A, Hitomi J, Germscheid M, Ch'en IL, Korkina O, Teng X, et al. Identification of RIP1 kinase as a specific cellular target of necrostatins. Nat Chem Biol. 2008;4:313.
4. Polykratis A, Hermance N, Zelic M, Roderick J, Kim C, Van T-M, et al. Cutting edge: RIPK1 Kinase inactive mice are viable and protected from TNF-induced necroptosis in vivo. J Immunol. 2014;193:1539–43.
5. Ofengeim D, Ito Y, Najafov A, Zhang Y, Shan B, DeWitt JP, et al. Activation of necroptosis in multiple sclerosis. Cell Rep. 2015;10:1836–49.
6. Schwarzer R, Laurien L, Pasparakis M. New insights into the regulation of apoptosis, necroptosis, and pyroptosis by receptor interacting protein kinase 1 and caspase-8. Curr Opin Cell Biol. 2020;63:186–93.
7. Li J, McQuade T, Siemer AB, Napetschnig J, Moriwaki K, Hsiao Y-S, et al. The RIP1/RIP3 necrosome forms a functional amyloid signaling complex required for programmed necrosis. Cell. 2012;150:339–50.
8. He S, Wang L, Miao L, Wang T, Du F, Zhao L, et al. Receptor interacting protein kinase-3 determines cellular necrotic response to TNF-alpha. Cell. 2009;137:1100–11.
9. Cho YS, Challa S, Moquin D, Genga R, Ray TD, Guildford M, et al. Phosphorylation-driven assembly of the RIP1-RIP3 complex regulates programmed necrosis and virus-induced inflammation. Cell. 2009;137:1112–23.
10. Sun L, Wang H, Wang Z, He S, Chen S, Liao D, et al. Mixed lineage kinase domain-like protein mediates necrosis signaling downstream of RIP3 kinase. Cell. 2012;148:213–27.
11. Liu S, Liu H, Johnston A, Hanna-Addams S, Reynoso E, Xiang Y, et al. MLKL forms disulfide bond-dependent amyloid-like polymers to induce necroptosis. Proc Natl Acad Sci USA. 2017;114:E7450–E9.
12. Murphy JM, Czabotar PE, Hildebrand JM, Lucet IS, Zhang JG, Alvarez-Diaz S, et al. The pseudokinase MLKL mediates necroptosis via a molecular switch mechanism. Immunity. 2013;39:443–53.
13. Patel S, Webster JD, Varfolomeev E, Kwon YC, Cheng JH, Zhang J, et al. RIP1 inhibition blocks inflammatory diseases but not tumor growth or metastases. Cell Death Differ. 2020;27:161–75.
14. Newton K, Dugger D, Maltzman A, Greve J, Hedehus M, Martin-McNulty B, et al. RIPK3 deficiency or catalytically inactive RIPK1 provides greater benefit than MLKL deficiency in mouse models of inflammation and tissue injury. Cell Death Differ. 2016;23:1565–76.
15. Lule S, Wu L, McAllister LM, Edmiston WJ III, Chung JY, Levy E, et al. Genetic inhibition of RIPK1 reduces cell death and improves functional outcome after intracerebral hemorrhage in mice. Stroke 2017;48:2549.
16. Datta A, Sarmah D, Mounica L, Kaur H, Kesharwani R, Verma G, et al. Cell death pathways in ischemic stroke and targeted pharmacotherapy. Transl Stroke Res. 2020:1–18. https://doi.org/10.1007/s12975-020-00806-z.
17. Chen T, Pan H, Li J, Xu H, Jin H, Qian C, et al. Inhibiting of RIPK3 attenuates early brain injury following subarachnoid hemorrhage: possibly through alleviating necroptosis. Biomedicine Pharmacother. 2018;107:563–70.
18. Wang Y, Wang H, Tao Y, Zhang S, Wang J, Feng X. Necroptosis inhibitor necrostatin-1 promotes cell protection and physiological function in traumatic spinal cord injury. Neuroscience. 2014;266:91–101.
19. Zhu S, Zhang Y, Bai G, Li H. Necrostatin-1 ameliorates symptoms in R6/2 transgenic mouse model of Huntington's disease. Cell Death Dis. 2011;2:e115–e.
20. Ofengeim D, Mazzitelli S, Ito Y, DeWitt JP, Mifflin L, Zou C, et al. RIPK1 mediates a disease-associated microglial response in Alzheimer's disease. Proc Natl Acad Sci USA. 2017;114:E8788–E97.
21. Caccamo A, Branca C, Piras IS, Ferreira E, Huentelman MJ, Liang WS, et al. Necroptosis activation in Alzheimer's disease. Nat Neurosci. 2017;20:1236.
22. Iannielli A, Bido S, Folladori L, Segnali A, Cancellieri C, Maresca A, et al. Pharmacological inhibition of necroptosis protects from dopaminergic neuronal cell death in Parkinson's disease models. Cell Rep. 2018;22:2066–79.
23. Xu D, Jin T, Zhu H, Chen H, Ofengeim D, Zou C, et al. TBK1 suppresses RIPK1-driven apoptosis and inflammation during development and in aging. Cell. 2018;174:1477–91. e19
24. Re DB, Le Verche V, Yu C, Amoroso MW, Politi KA, Phani S, et al. Necroptosis drives motor neuron death in models of both sporadic and familial ALS. Neuron. 2014;81:1001–8.

25. Ito Y, Ofengeim D, Najafov A, Das S, Saberi S, Li Y, et al. RIPK1 mediates axonal degeneration by promoting inflammation and necroptosis in ALS. Science. 2016;353:603–8.
26. Yoshikawa M, Saitoh M, Katoh T, Seki T, Bigi SV, Shimizu Y, et al. Discovery of 7-oxo-2, 4, 5, 7-tetrahydro-6 H-pyrazolo [3, 4-c] pyridine derivatives as potent, orally available, and brain-penetrating receptor interacting protein 1 (RIP1) kinase inhibitors: analysis of structure–kinetic relationships. J Med Chem. 2018;61:2384–409.
27. Webster JD, Vucic D. The balance of TNF mediated pathways regulates inflammatory cell death signaling in healthy and diseased tissues. Front Cell Dev Biol. 2020;8:365.
28. Taylor JP, Brown RH, Cleveland DW. Decoding ALS: from genes to mechanism. Nature 2016;539:197–206.
29. Dermentzaki G, Politi KA, Lu L, Mishra V, Pérez-Torres EJ, Sosunov AA, et al. Deletion of Ripk3 prevents Motor Neuron death in vitro but not in vivo. eneuro. 2019;6:ENEURO.0308-18.2018.
30. Maruyama H, Morino H, Ito H, Izumi Y, Kato H, Watanabe Y, et al. Mutations of optineurin in amyotrophic lateral sclerosis. Nature. 2010;465:223–6.
31. Pottier C, Bieniek KF, Finch N, van de Vorst M, Baker M, Perkersen R, et al. Whole-genome sequencing reveals important role for TBK1 and OPTN mutations in frontotemporal lobar degeneration without motor neuron disease. Acta Neuropathologica. 2015;130:77–92.
32. Feng SM, Che CH, Feng SY, Liu CY, Li LY, Li YX, et al. Novel mutation in optineurin causing aggressive ALS+/− frontotemporal dementia. Annals of Clinical and Translational. Neurology 2019;6:2377–83.
33. Freischmidt A, Wieland T, Richter B, Ruf W, Schaeffer V, Müller K, et al. Haploinsufficiency of TBK1 causes familial ALS and fronto-temporal dementia. Nat Neurosci. 2015;18:631–6.
34. Rosen DR, Siddique T, Patterson D, Figlewicz DA, Sapp P, Hentati A, et al. Mutations in Cu/Zn superoxide dismutase gene are associated with familial amyotrophic lateral sclerosis. Nature 1993;362:59–62.
35. Philips T, Rothstein JD. Rodent models of amyotrophic lateral sclerosis. Curr Protoc Pharmacol. 2015;69:1–5. 21
36. Wang T, Perera ND, Chiam MD, Cuic B, Wanniarachchillage N, Tomas D, et al. Necroptosis is dispensable for motor neuron degeneration in a mouse model of ALS. Cell Death Differ. 2019;27:1728–39.
37. Mandal P, Berger SB, Pillay S, Moriwaki K, Huang C, Guo H, et al. RIP3 induces apoptosis independent of pronecrotic kinase activity. Mol Cell. 2014;56:481–95.
38. Newton K, Dugger DL, Wickliffe KE, Kapoor N, de Almagro MC, Vucic D, et al. Activity of protein kinase RIPK3 determines whether cells die by necroptosis or apoptosis. Science. 2014;343:1357–60.
39. Gurney ME, Pu H, Chiu AY, Dal Canto MC, Polchow CY, Alexander DD, et al. Motor neuron degeneration in mice that express a human Cu,Zn superoxide dismutase mutation. Science. 1994;264:1772–5.
40. Sengupta-Ghosh A, Dominguez SL, Xie L, Barck KH, Jiang Z, Earr T, et al. Muscle specific kinase (MuSK) activation preserves neuromuscular junctions in the diaphragm but is not sufficient to provide a functional benefit in the SOD1G93A mouse model of ALS. Neurobiol Dis. 2019;124:340–52.
41. de Almagro MC, Goncharov T, Izrael-Tomasevic A, Duttler S, Kist M, Varfolomeev E, et al. Coordinated ubiquitination and phosphorylation of RIP1 regulates necroptotic cell death. Cell Death Differ. 2017;24:26–37.
42. Le Pichon CE, Meilandt WJ, Dominguez S, Solanoy H, Lin H, Ngu H, et al. Loss of dual leucine zipper kinase signaling is protective in animal models of neurodegenerative disease. Sci Transl Med. 2017;9:eaag0394.
43. Veta M, Van Diest PJ, Kornegoor R, Huisman A, Viergever MA, Pluim JP. Automatic nuclei segmentation in H&E stained breast cancer histopathology images. PloS One. 2013;8:e70221.
44. De Olmos JS, Beltramino CA, De Lorenzo SDO. Use of an amino-cupric-silver technique for the detection of early and semiacute neuronal degeneration caused by neurotoxicants, hypoxia, and physical trauma. Neurotoxicology Teratol. 1994;16:545–61.
45. Zendedel A, Beyer C, Kipp M. Cuprizone-induced demyelination as a tool to study remyelination and axonal protection. J Mol Neurosci. 2013;51:567–72.
46. Kang SH, Li Y, Fukaya M, Lorenzini I, Cleveland DW, Ostrow LW, et al. Degeneration and impaired regeneration of gray matter oligodendrocytes in amyotrophic lateral sclerosis. Nat Neurosci. 2013;16:571.
47. Philips T, Bento-Abreu A, Nonneman A, Haeck W, Staats K, Geelen V, et al. Oligodendrocyte dysfunction in the pathogenesis of amyotrophic lateral sclerosis. Brain. 2013;136:471–82.
48. Khalil M, Teunissen CE, Otto M, Piehl F, Sormani MP, Gattringer T, et al. Neurofilaments as biomarkers in neurological disorders. Nat Rev Neurol. 2018;14:577–89.
49. Mejzini R, Flynn LL, Pitout IL, Fletcher S, Wilton SD, Akkari PA. ALS genetics, mechanisms, and therapeutics: where are we now? Front Neurosci. 2019;13:1310. https://doi.org/10.3389/fnins.2019.01310.
50. Jagmag SA, Tripathi N, Shukla SD, Maiti S, Khurana S. Evaluation of models of Parkinson's disease. Front Neurosci. 2016;9:503.
51. Dionísio PA, Oliveira SR, Gaspar MM, Gama MJ, Castro-Caldas M, Amaral JD, et al. Ablation of RIP3 protects from dopaminergic neurodegeneration in experimental Parkinson's disease. Cell Death Dis. 2019;10:1–14.
52. Lin Q-S, Chen P, Wang W-X, Lin C-C, Zhou Y, Yu L-H, et al. RIP1/RIP3/MLKL mediates dopaminergic neuron necroptosis in a mouse model of Parkinson disease. Lab Investig. 2019;100:503–11.
53. Zhang Y, Chen K, Sloan SA, Bennett ML, Scholze AR, O'Keeffe S, et al. An RNA-sequencing transcriptome and splicing database of glia, neurons, and vascular cells of the cerebral cortex. J Neurosci. 2014;34:11929–47.
54. Wu J, Huang Z, Ren J, Zhang Z, He P, Li Y, et al. Mlkl knockout mice demonstrate the indispensable role of Mlkl in necroptosis. Cell Res. 2013;23:994–1006.
55. Kanno H, Ozawa H, Tateda S, Yahata K, Itoi E. Upregulation of the receptor-interacting protein 3 expression and involvement in neural tissue damage after spinal cord injury in mice. BMC Neurosci. 2015;16:62.
56. Webster JD, Kwon YC, Park S, Zhang H, Corr N, Ljumanovic N, et al. RIP1 kinase activity is critical for skin inflammation but not for viral propagation. J Leukoc Biol. 2020;107:941–52.
57. Vlantis K, Wullaert A, Polykratis A, Kondylis V, Dannappel M, Schwarzer R, et al. NEMO prevents RIP kinase 1-mediated epithelial cell death and chronic intestinal inflammation by NF-κB-dependent and-independent functions. Immunity. 2016;44:553–67.
58. Berger SB, Kasparcova V, Hoffman S, Swift B, Dare L, Schaeffer M, et al. Cutting Edge: RIP1 kinase activity is dispensable for normal development but is a key regulator of inflammation in SHARPIN-deficient mice. J Immunol. 2014;192:5476–80.
59. Rickard JA, Anderton H, Etemadi N, Nachbur U, Darding M, Peltzer N, et al. TNFR1-dependent cell death drives inflammation in Sharpin-deficient mice. Elife. 2014;3:e03464.

60. Morrice JR, Gregory-Evans CY, Shaw CA. Animal models of amyotrophic lateral sclerosis: a comparison of model validity. Neural regeneration Res. 2018;13:2050.
61. Mackenzie IR, Bigio EH, Ince PG, Geser F, Neumann M, Cairns NJ, et al. Pathological TDP-43 distinguishes sporadic amyotrophic lateral sclerosis from amyotrophic lateral sclerosis with SOD1 mutations. Ann Neurol. 2007;61:427–34.
62. Garbuzova-Davis S, Sanberg PR. Blood-CNS barrier impairment in ALS patients versus an animal model. Front Cell Neurosci. 2014;8:21.
63. Garbuzova-Davis S, Kurien C, Thomson A, Falco D, Ahmad S, Staffetti J, et al. Endothelial and astrocytic support by human bone marrow stem cell grafts into symptomatic ALS mice towards blood-spinal cord barrier repair. Sci Rep. 2017;7:884.
64. Garbuzova-Davis S, Ehrhart J, Mustafa H, Llauget A, Boccio KJ, Sanberg PR, et al. Phenotypic characteristics of human bone marrow-derived endothelial progenitor cells in vitro support cell effectiveness for repair of the blood-spinal cord barrier in ALS. Brain Res. 2019;1724:146428.
65. Yu X, Mao M, Liu X, Shen T, Li T, Yu H, et al. A cytosolic heat shock protein 90 and co-chaperone p23 complex activates RIPK3/MLKL during necroptosis of endothelial cells in acute respiratory distress syndrome. J Mol Med. 2020;98:569–83.
66. Chen A-Q, Fang Z, Chen X-L, Yang S, Zhou Y-F, Mao L, et al. Microglia-derived TNF-α mediates endothelial necroptosis aggravating blood brain–barrier disruption after ischemic stroke. Cell Death Dis. 2019;10:1–18.
67. Zelic M, Roderick JE, O'Donnell JA, Lehman J, Lim SE, Janardhan HP, et al. RIP kinase 1–dependent endothelial necroptosis underlies systemic inflammatory response syndrome. J Clin Investig. 2018;128:2064–75.